Intrinsic topological property for precise structure differentiation

Tie Yang,[1,*] Min-Quan Kuang,[1,*] Xiaoming Zhang,[2,†] Weikang Wu,[3,4,‡] and Zhi-Ming Yu[5]

[1]*School of Physical Science and Technology, Southwest University, Chongqing 400715, China*

[2]*School of Materials Science and Engineering, Hebei University of Technology, Tianjin 300130, China*

[3]*Key Laboratory for Liquid-Solid Structural Evolution and Processing of Materials (Ministry of Education), Shandong University, Jinan, Shandong 250061, China*

[4]*Research Laboratory for Quantum Materials, Singapore University of Technology and Design, Singapore 487372, Singapore*

[5]*Key Laboratory of Advanced Optoelectronic Quantum Architecture and Measurement (MOE), Beijing Key Laboratory of Nanophotonics & Ultrafine Optoelectronic Systems, and School of Physics, Beijing Institute of Technology, Beijing 100081, China*

(Received 30 June 2022; accepted 3 April 2023; published 25 April 2023)

Topology in condensed matter systems, inherited from the crystalline symmetry, has aroused great research interest in recent years, yet most studies are focused on the theoretical conceptual perspective and experimental verification. Herein, we present a practical application direction of the topological orders, as the intrinsic properties of the crystalline symmetry, for precise structural differentiation. Based on first-principles calculations, we studied the electronic bands and topological properties of α-nitrogen under the long contradictory structures $P2_13$ and $Pa\bar{3}$. Their comparable band structures come from their great crystal structure similarity, together leading to the difficulty of precise structural determination from conventional techniques. However, when we look at the intrinsic topology from these two structures, a strong different topological feature is observed between them. A large chiral Fermi arc state is present in the $P2_13$ structure, connecting the triple point at Γ and the Dirac point at R, whereas there is no such arc state in the $Pa\bar{3}$ structure. Indeed, this Fermi arc state in the $P2_13$ structure corresponds to one of two arc states from the ± 2 topological charge points at the Γ and R points, where the triple point and Dirac point do not carry any charge in $Pa\bar{3}$ because of its centrosymmetric symmetry. This distinct topological behavior between these two structures can provide a definitive means for its final structure determination.

DOI: 10.1103/PhysRevB.107.155138

I. INTRODUCTION

Recently, the study of topological properties in condensed matter systems has aroused great research interest in the field of solid state physics [1–5]. The emergent low-energy quasiparticles in solid states, which originate from the intrinsic topological order of the crystalline structure, can exotically serve as analogs of the elementary particles in high-energy physics, and therefore can provide effective platforms to examine the related fundamental physics. With continuous effort and development, great achievements have been realized and, in particular, since the topological band theory was established [6–8], many more unconventional topological quasiparticles have been predicated beyond the conventional Weyl, Dirac, and Majorana particles under Poincaré symmetry. These quasiparticles in solid states can show different pseudospin structures, topological charges, dispersion types, and various topological manifolds. The current study of crystal topology has even been further extended to phonons [9–14], photons [15,16], and magnons [17–19], which are bosons compared with their electronic fermion counterparts.

Up to now, nontrivial surface states, as the major feature of topological properties, are often used in both theoretical calculations and experimental characterizations for the determination of the corresponding topological states [20–30]. For topological nodal points, the Fermi arc spectrum originates from the crossing points; for topological nodal lines or loops, the drumhead surface states are formed between the crossing lines or within the crossing loops. Indeed, these nontrivial surface states are the real fundamental aspects for the topological properties in crystal space group symmetries and they provide future potentials for new quantum devices and applications. However, even with consistent development for more than a decade, current research of the topological properties in crystals is still primarily focused on the basic science and only a few conceptual prototypes for the application of topological states have been presented. Especially, most experimental studies have concentrated on the verification of theoretical predictions for some specific topological element in some material systems, which is still far from the final application aim.

In this paper, we elaborate on a different perspective of the topological properties of crystal materials for practical purposes. As the topological states are intrinsically inherited

*These authors contributed equally to this work.

†zhangxiaoming87@hebut.edu.cn

‡weikang_wu@sdu.edu.cn

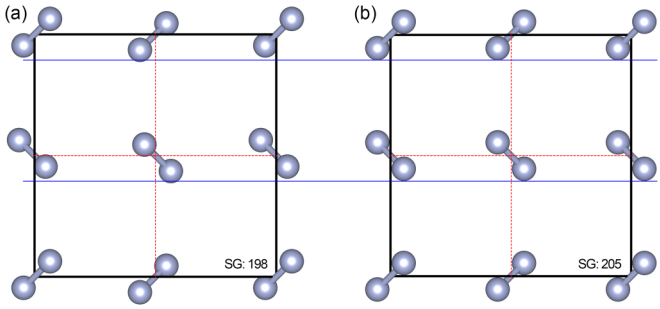

FIG. 1. The crystal structures of α-nitrogen between two cubic space groups $P2_13$ (SG 198) and $Pa\bar{3}$ (SG 205). The two color lines are overlaid for better visualization of the difference between the two structures.

from the crystal symmetry, they can thus be used in a reverse manner for the determination of the crystal symmetry. This thought seems a little bit confusing but it appears to be very interesting and useful for the precise differentiation of the crystal structures with very similar symmetries. For example, for the solid phase crystals α-nitrogen and α-carbon monoxide [31–33], there is a long-standing controversy regarding their structure determination between two cubic space groups $P2_13$ (No. 198) and $Pa\bar{3}$ (No. 205). Taking α-nitrogen as an example, its crystal structures under these two space groups are shown in Fig. 1, where the two color lines are overlaid for better visualization of the difference between the two structures. We can see that these two structures are almost identical and only a slight position variation of the nitrogen molecule can be carefully observed. It should be noted that the space group $Pa\bar{3}$ is centrosymmetric, where the center of the nitrogen molecule locates exactly at the origin, whereas the other one $P2_13$ is noncentrosymmetric, where the center of the nitrogen molecule has a very small offset from the origin. Because of this extreme structural similarity, different experimental techniques have been employed for its structure analysis, including x-ray diffraction [34], electron diffraction [35], neutron diffraction [36], infrared spectrometry [37], and Raman spectrometry [32]. However, the results from different techniques exhibit inconsistencies and discrepancies, and the final structure still remains unsolved.

II. COMPUTATIONAL METHODS

In this paper, based on theoretical calculations and an effective model analysis, we present a practical application of the topological property for precise α-nitrogen structure determination. First-principles calculations have been performed under the framework of density functional theory (DFT) [38] as implemented within the Vienna *ab initio* simulation package [39]. The projector augmented-wave (PAW) method is used for the interactions between valence electrons and ions [40], and the Perdew-Burke-Ernzerhof (PBE) functional is selected to deal with the exchange correlation energy [41]. Based on a convergence test, a cutoff energy of 520 eV is set for the plane wave and a Monkhorst-Pack grid of $6 \times 6 \times 6$ k mesh is sampled for the full Brillouin zone. The crystal structure is fully relaxed until the residual total force per atom is less than 1×10^{-3} eV/Å and the derived

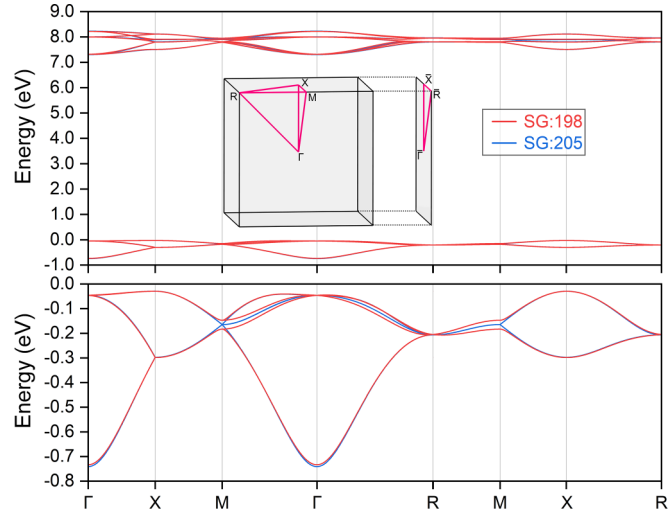

FIG. 2. The calculated electronic band structures for the α-nitrogen under different structural configurations on the top panel, where the inset illustrates the bulk and projected (001) surface Brillouin zone with high symmetric points and paths labeled. The local bands around the Fermi energy are shown on the bottom, in which several band configuration differences can be observed.

lattice constants are $a = b = c = 5.87$ Å for the $P2_13$ structure and $a = b = c = 5.86$ Å for the $Pa\bar{3}$ structure, which are in very good agreement with previous experimental results [34,35,42–44].

III. RESULTS AND DISCUSSION

Based on these optimized crystal structures, the electronic band structures are calculated and exhibited in Fig. 2, in which the Fermi energy has been shifted to 0 eV. Note that we did not consider the spin orbital coupling (SOC) effect here since only the light element N is involved and we will further discuss it later. We can observe that the electronic bands under the two structures are nearly identical since they are almost overlapped and only a very small difference can be found from the local band enlargement near the Fermi energy level. These tiny band differences are only located at some specific high symmetric points and paths; furthermore, they are also deeply buried within the large energy range of the band span. These similar band structures are caused by similar crystal structures, and they together render the great hardship of the precise structure determination for α-nitrogen, even from different theoretical perspectives and experimental characterizations [31,32,35,36,42,43,45].

However, we get some clarification when we trace back these band differences to their intrinsic topological properties under the two different structures. The local band differences, as shown on the bottom panel of Fig. 2, are focused on the band crossings and degeneracies at the M point or along the M-Γ-R-M path. For example, the four bands, which form two doubly degenerate points at the M point under the $P2_13$ [space group (SG) 198] structure, cross into a single quadruply degenerate or Dirac point under the $Pa\bar{3}$ (No. 205) structure; the different bands, which are separated along the M-Γ, Γ-R, and R-M paths under the $P2_13$ (SG 198) structure, converge

into a doubly or quadruply degenerate band under the $Pa\bar{3}$ (No. 205) structure. Notably, for both $P2_13$ and $Pa\bar{3}$, there is a threefold degenerate point at Γ, close to 10 meV below the Fermi energy. At R, the bands for $P2_13$ feature a fourfold degenerate point at about 200 meV below the Fermi energy, while it becomes a part of a Dirac nodal line on M-R for $Pa\bar{3}$.

The band differences between the two types of crystal structures are dictated by their distinct crystalline symmetries and the time reversal $\mathcal{T}$. For the crystal structure with the $P2_13$ space group (No. 198), the symmetry operations include threefold rotations C_3 along the $\langle 111\rangle$ direction, and three perpendicular twofold screw rotations $\tilde{C}_{2x} \equiv \{C_{2x}|\frac{1}{2}\frac{1}{2}0\}$, $\tilde{C}_{2y} \equiv \{C_{2y}|0\frac{1}{2}\frac{1}{2}\}$, and $\tilde{C}_{2z} \equiv \{C_{2z}|\frac{1}{2}0\frac{1}{2}\}$, along the $\langle 100\rangle$ axes. In comparison, the space group $Pa\bar{3}$ (No. 205) is a supergroup of SG 198, with an extra inversion symmetry $\mathcal{P}$. For these two structure types, such a difference will lead to dissimilar band features and topological properties of the band crossings, especially at points Γ and R, as well as along the M-R path. First, for the $P2_13$ structure, the triply degenerate point at Γ is guaranteed to be of spin-1 type [46], that is, $\mathcal{H}_{\mathrm{TP}}^{P2_13}(\boldsymbol{k}) \propto \boldsymbol{k}\cdot\boldsymbol{S}$ with S_i the spin-1 matrix representations of rotation generators. It features linear band splitting along all directions in the momentum space, and carries a nonzero Chern number $C = 2, 0, -2$ for three bands, respectively. However, for $Pa\bar{3}$, the inclusion of $\mathcal{P}$ eliminates the linear term of the effective Hamiltonian, and transforms the spin-1 point to a quadratic contact triple point (QCTP) with quadratic energy dispersion along all directions. Noting that it is formed by a linear crossing between a doubly degenerate band and a nondegenerate band along certain high-symmetry lines, the QCTP does not have a well-defined Chern number. Second, the crystal structure with $P2_13$ hosts a Dirac point at R. It is stabilized by the anticommutation relations among the three twofold screw rotations, in combination with $\mathcal{T}$, and its effective Hamiltonian can be expressed as (up to the linear order),

$$\mathcal{H}_{\mathrm{DP}}^{P2_13}(\boldsymbol{k}) \propto \begin{bmatrix} k_x\sigma_x - k_y\sigma_y - k_z\sigma_z & 0 \\ 0 & -k_x\sigma_x - k_y\sigma_y + k_z\sigma_z \end{bmatrix}, \tag{1}$$

where $\boldsymbol{k}$ is measured from the Dirac point, σ_i are Pauli matrices, and c_i are real model parameters. This model indicates that the Dirac point consists of two linear Weyl points with the same chirality; in other words, it is a charge-2 Dirac point with nonzero topological charges of ± 2. In contrast, for the $Pa\bar{3}$ structure, owing to $\mathcal{PT}$, the Dirac point at R is no longer an isolated point but resides on the Dirac nodal line, as discussed in the next point. Third, the twofold degeneracy along M-R for the $P2_13$ structure will be doubled under the higher-symmetry $Pa\bar{3}$. Both $P2_13$ and $Pa\bar{3}$ host the antiunitary symmetries $\mathcal{T}\tilde{C}_{2i}$ with $i = x, y$, which ensures two perpendicular nodal surfaces at the boundary of Brillouin zone, i.e., the $k_{x/y} = \pi$ planes, due to $(\mathcal{T}\tilde{C}_{2i})^2 = -1$. The path M-R is located at the intersection of two nodal surfaces. This explains the double degeneracy for $P2_13$. For $Pa\bar{3}$, however, $\mathcal{PT}$ would glue together two doubly degenerate states along M-R to form a Dirac nodal line.

These topological band crossings are characterized by nontrivial surface states and, to obtain the topological surface states for α-nitrogen under both structures, a Wannier tight-binding Hamiltonian has been established based on the maximally localized Wannier functions as projected from the bulk Bloch wave functions [47,48]. A surface slab model has been constructed along the (001) surface and the calculated electronic local density of the surface states for both structures are shown in Fig. 3, and the corresponding surface path can be referred to Fig. 2. The surface spectra of both structures are very similar and these surface band distributions are consistent with their bulk band structure. A small gap area is present along $\bar{\Gamma}$-$\bar{X}$-$\bar{R}$ in the $P2_13$ (SG 198) structure, and this is from the gap of the multiple nondegenerate bands in the bulk phase, as shown by the bulk band overlays; see Fig. S1 in the Supplemental Material [49]. Interestingly, a large Fermi arc surface state is observed within this gap as indicated by the red arrow in Fig. 3(b) and it connects the triple point at $\bar{\Gamma}$

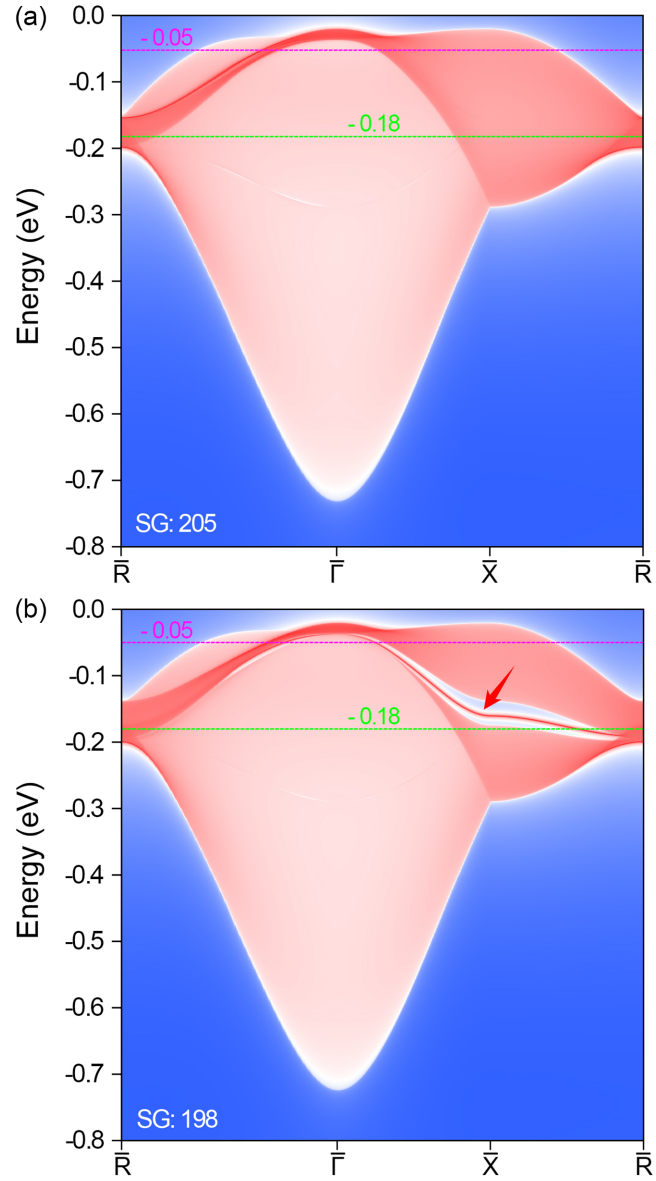

FIG. 3. The calculated electronic surface states on the (001) surface for the α-nitrogen under the $Pa\bar{3}$ (SG 205) structure (a) and the $P2_13$ (SG 198) structure (b). A large Fermi arc state connects $\bar{\Gamma}$ and $\bar{R}$ points as indicated by the red arrow in the $P2_13$ (SG 198) structure (b).

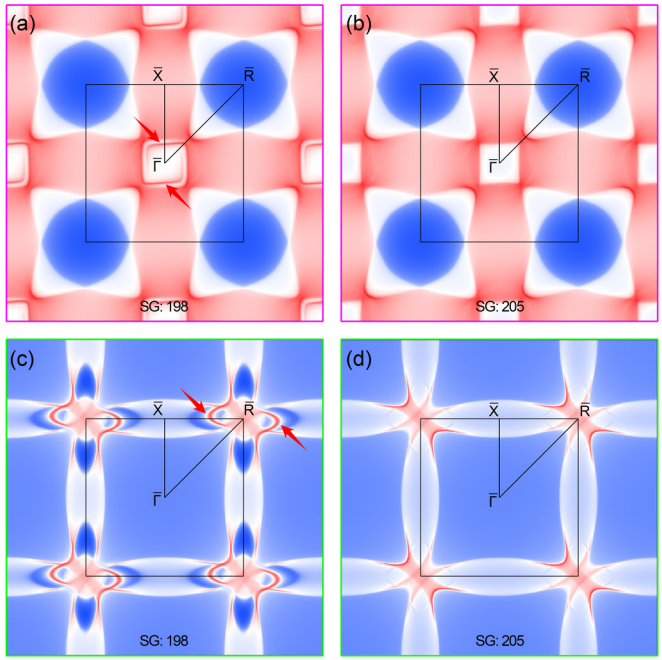

FIG. 4. The calculated electronic surface contours on the (001) surface at two energy values for α-nitrogen under $P2_13$ (SG 198) and $Pa\bar{3}$ (SG 205) structures. The Fermi arc states are marked by the red arrows for the $P2_13$ (SG 198) structure. The surface Brillouin zone paths are overlaid by the black lines. The color border lines for the surface contours correspond to the constant energy values of -0.05 and -0.18 eV as referred to in Fig. 3.

and the Dirac point at $\bar{R}$ along the $\bar{\Gamma}$-$\bar{X}$-$\bar{R}$ path. This Fermi arc is stable in a large energy window and spatial distribution, which is very beneficial for its further experimental detection. A closer look can find another small gap along the $\bar{R}$-$\bar{\Gamma}$ path, in which a small Fermi arc also emerges from the triple point at $\bar{\Gamma}$.

As we discussed above, the triple point and the Dirac point at Γ and R carry ± 2 topological charges in the $P2_13$ (SG 198) structure, and we thus further calculated the Fermi surface contours on the (001) surface at two constant energies, as denoted by the two colored dashed lines in Fig. 3, and the results are reported in Fig. 4. In addition, we also plot the same surface contours for the $Pa\bar{3}$ (No. 205) structure. We can see both structures exhibit very similar surface contour distributions for the two selected energy values and a major difference is the double Fermi arc states around the $\bar{\Gamma}$ point at -0.05 eV and around the $\bar{R}$ point at -0.18 eV, as indicated by the arrows in the figure. Further scans of the surface contour at smaller energy intervals find these two Fermi arc states at the $\bar{\Gamma}$ and $\bar{R}$ points are connected together and they are emitted from the triple point at $\bar{\Gamma}$, ending in a Dirac point at $\bar{R}$, which is consistent with their topological charge properties. The precise surface contour evolution with scan energy variations is assembled in a short video and several selected surface contour figures at different energy values for both space groups are plotted in Figs. S2 and S3 of the Supplemental Material [49], which can further confirm the above analysis about the origin of the surface arc state. Since the SOC is not considered in the above discussion, we need to further check its effect. The obtained band structures and surface states of the α-nitrogen under both structures with SOC are reported in Figs. S4 and S5 of the Supplemental Material [49], and we can see that the SOC effect does not have any impact and the band structures and surface states remain the same as that without SOC, which can be simply understood because the only element N is very light. Thus, the SOC effect does not vary the above analysis and our results. In addition, to compensate for the possible intermolecular forces in the α-nitrogen crystal, we further check the band structures by considering the van der Waals (vdW) interaction and the calculated bands with the state-of-art vdW energy correction method DFT-D3 and DFT-D4 are displayed in Figs. S6 and S7 of the Supplemental Material [49], and we can find the same band configurations with the PBE method, especially for the difference in the topological features between these two structures.

IV. CONCLUSION

Based on first-principles calculations, we studied the electronic bands and topological properties of α-nitrogen under the long contradictory structures $P2_13$ and $Pa\bar{3}$. Their similar band structures come from a great crystal structure similarity, together leading to the difficulty of precise structural determination from conventional techniques. However, when we come to the intrinsic topology from these two structures, a strong different topological feature is observed between them. A large chiral Fermi arc state is present in the $P2_13$ structure, connecting the triple point at Γ and the Dirac point at R, whereas there is no such arc state in the $Pa\bar{3}$ structure. Indeed, this chiral Fermi arc state in the $P2_13$ structure corresponds to one of two arc states from the ± 2 topological charge points at the Γ and R points, where the triple point and Dirac point do not carry any charge in $Pa\bar{3}$ because of its centrosymmetric symmetry. This distinct topological behavior between these two structures can provide a definitive way for its final structure determination and, with the great enhancement in the detection technology and devices, such as the 1 meV energy resolution of laser-based angle-resolved photoemission spectroscopy (ARPES) [50] and cryogenic scanning tunneling microscopy (CSTM) [51], the corresponding experimental characterization can be immediately advanced. Specifically, the distinct topological features of the top valence bands can be easily detected by the ARPES and the chiral surface states can also be accurately detected [52]. Compared with previous theoretical and experimental works, this study offers a real application of the topological properties from crystal symmetry for practical purposes.

ACKNOWLEDGMENTS

We acknowledge financial support from the Natural Science Foundation of Chongqing (Grant No. cstc2021jcyj-msxmX0376) and the National Natural Science Foundation of China (Grant No. 11704315). W.W. is thankful for the Special Funding in the Project of Qilu Young Scholar Program of Shandong University. The authors wish to acknowledge the high-performance computing platform of School of Physical Science and Technology of Southwest University for computational resources support.

[1] M. Z. Hasan and C. L. Kane, Rev. Mod. Phys. **82**, 3045 (2010).
[2] N. P. Armitage, E. J. Mele, and A. Vishwanath, Rev. Mod. Phys. **90**, 015001 (2018).
[3] A. Bansil, H. Lin, and T. Das, Rev. Mod. Phys. **88**, 021004 (2016).
[4] J. Xiao and B. Yan, Nat. Rev. Phys. **3**, 283 (2021).
[5] T. Zhang, Y. Jiang, Z. Song, H. Huang, Y. He, Z. Fang, H. Weng, and C. Fang, Nature (London) **566**, 475 (2019).
[6] F. Tang, H. C. Po, A. Vishwanath, and X. Wan, Nature (London) **566**, 486 (2019).
[7] F. Tang, H. C. Po, A. Vishwanath, and X. Wan, Nat. Phys. **15**, 470 (2019).
[8] Z. Yu, Z. Zhang, G.-B. Liu, W. Wu, X.-P. Li, R.-w. Zhang, S. Yang, and Y. Yao, Sci. Bull. **67**, 375 (2022).
[9] N. R. Cooper, J. Dalibard, and I. B. Spielman, Rev. Mod. Phys. **91**, 015005 (2019).
[10] Y. Yang, J.-p. Xia, H.-x. Sun, Y. Ge, D. Jia, S.-q. Yuan, S. A. Yang, Y. Chong, and B. Zhang, Nat. Commun. **10**, 5185 (2019).
[11] Y. Long, J. Ren, and H. Chen, Phys. Rev. Lett. **124**, 185501 (2020).
[12] R. Wang, B. W. Xia, Z. J. Chen, B. B. Zheng, Y. J. Zhao, and H. Xu, Phys. Rev. Lett. **124**, 105303 (2020).
[13] B. W. Xia, R. Wang, Z. J. Chen, Y. J. Zhao, and H. Xu, Phys. Rev. Lett. **123**, 065501 (2019).
[14] Z.-K. Lin, Y. Wu, B. Jiang, Y. Liu, S.-Q. Wu, F. Li, and J.-H. Jiang, Nat. Mater. **21**, 430 (2022).
[15] B. Yang, Q. Guo, B. Tremain, R. Liu, L. E. Barr, Q. Yan, W. Gao, H. Liu, Y. Xiang, J. Chen, C. Fang, A. Hibbins, L. Lu, and S. Zhang, Science **359**, 1013 (2018).
[16] Y. Liu, S. Leung, F.-F. Li, Z.-K. Lin, X. Tao, Y. Poo, and J.-H. Jiang, Nature (London) **589**, 381 (2021).
[17] K. Li, C. Li, J. Hu, Y. Li, and C. Fang, Phys. Rev. Lett. **119**, 247202 (2017).
[18] S. Nie, Y. Sun, F. B. Prinz, Z. Wang, H. Weng, Z. Fang, and X. Dai, Phys. Rev. Lett. **124**, 076403 (2020).
[19] F. Zhu, L. Zhang, X. Wang, F. J. d. Santos, J. Song, T. Mueller, K. Schmalzl, W. F. Schmidt, A. Ivanov, J. T. Park, J. Xu, J. Ma, S. Lounis, S. Blügel, Y. Mokrousov, Y. Su, and T. Brückel, Sci. Adv. **7**, eabi7532 (2021).
[20] S.-Y. Xu, I. Belopolski, N. Alidoust, M. Neupane, G. Bian, C. Zhang, R. Sankar, G. Chang, Z. Yuan, C.-C. Lee, S.-M. Huang, H. Zheng, J. Ma, D. S. Sanchez, B. Wang, A. Bansil, F. Chou, P. P. Shibayev, H. Lin, S. Jia *et al.*, Science **349**, 613 (2015).
[21] M. Xiao, L. Ye, C. Qiu, H. He, Z. Liu, and S. Fan, Sci. Adv. **6**, eaav2360 (2020).
[22] S.-Y. Xu, C. Liu, S. K. Kushwaha, R. Sankar, J. W. Krizan, I. Belopolski, M. Neupane, G. Bian, N. Alidoust, T.-R. Chang, H.-T. Jeng, C.-Y. Huang, W.-F. Tsai, H. Lin, P. P. Shibayev, F.-C. Chou, R. J. Cava, and M. Z. Hasan, Science **347**, 294 (2015).
[23] T. T. Zhang, H. Miao, Q. Wang, J. Q. Lin, Y. Cao, G. Fabbris, A. H. Said, X. Liu, H. C. Lei, Z. Fang, H. M. Weng, and M. P. M. Dean, Phys. Rev. Lett. **123**, 245302 (2019).
[24] R.-W. Zhang, Z. Zhang, C.-C. Liu, and Y. Yao, Phys. Rev. Lett. **124**, 016402 (2020).
[25] R. Yu, Q. Wu, Z. Fang, and H. Weng, Phys. Rev. Lett. **119**, 036401 (2017).
[26] D. Takane, Z. Wang, S. Souma, K. Nakayama, T. Nakamura, H. Oinuma, Y. Nakata, H. Iwasawa, C. Cacho, T. Kim, K. Horiba, H. Kumigashira, T. Takahashi, Y. Ando, and T. Sato, Phys. Rev. Lett. **122**, 076402 (2019).
[27] X.-L. Sheng, C. Chen, H. Liu, Z. Chen, Z.-M. Yu, Y. X. Zhao, and S. A. Yang, Phys. Rev. Lett. **123**, 256402 (2019).
[28] J. Hu, Z. Tang, J. Liu, X. Liu, Y. Zhu, D. Graf, K. Myhro, S. Tran, C. N. Lau, J. Wei, and Z. Mao, Phys. Rev. Lett. **117**, 016602 (2016).
[29] C. Chen, X.-T. Zeng, Z. Chen, Y. X. Zhao, X.-L. Sheng, and S. A. Yang, Phys. Rev. Lett. **128**, 026405 (2022).
[30] Z. J. Chen, R. Wang, B. W. Xia, B. B. Zheng, Y. J. Jin, Y.-J. Zhao, and H. Xu, Phys. Rev. Lett. **126**, 185301 (2021).
[31] W. N. Lipscomb, J. Chem. Phys. **60**, 5138 (1974).
[32] H. W. Löwen, K. D. Bier, and H. J. Jodl, J. Chem. Phys. **93**, 8565 (1990).
[33] W. B. J. M. Janssen, J. Michiels, and A. van der Avoird, J. Chem. Phys. **94**, 8402 (1991).
[34] T. H. Jordan, H. W. Smith, W. E. Streib, and W. N. Lipscomb, J. Chem. Phys. **41**, 756 (1964).
[35] J. A. Venables and C. A. English, Acta Crystallogr., Sect. B **30**, 929 (1974).
[36] H. E. Maynard-Casely, J. R. Hester, and H. E. A. Brand, IUCrJ **7**, 844 (2020).
[37] E. J. Wachtel, J. Chem. Phys. **57**, 5620 (1972).
[38] M. C. Payne, M. P. Teter, D. C. Allan, T. A. Arias, and J. D. Joannopoulos, Rev. Mod. Phys. **64**, 1045 (1992).
[39] J. Hafner, J. Comput. Chem. **29**, 2044 (2008).
[40] P. E. Blochl, Phys. Rev. B **50**, 17953 (1994).
[41] J. P. Perdew, K. Burke, and M. Ernzerhof, Phys. Rev. Lett. **77**, 3865 (1996).
[42] S. J. La Placa and W. C. Hamilton, Acta Crystallogr., Sect. B **28**, 984 (1972).
[43] B. Peigne and G. Aullon, Acta Crystallogr., Sect. B **71**, 369 (2015).
[44] K. Fujii, T. Fuka, H. Kondo, and K. Ishii, J. Phys. Soc. Jpn. **66**, 125 (1997).
[45] J. C. Raich, N. S. Gillis, and A. B. Anderson, J. Chem. Phys. **61**, 1399 (1974).
[46] P. Tang, Q. Zhou, and S.-C. Zhang, Phys. Rev. Lett. **119**, 206402 (2017).
[47] A. A. Mostofi, J. R. Yates, Y.-S. Lee, I. Souza, D. Vanderbilt, and N. Marzari, Comput. Phys. Commun. **178**, 685 (2008).
[48] Q. Wu, S. Zhang, H.-F. Song, M. Troyer, and A. A. Soluyanov, Comput. Phys. Commun. **224**, 405 (2018).
[49] See Supplemental Material at http://link.aps.org/supplemental/10.1103/PhysRevB.107.155138 for further information about the the electronic band structures and the topological surface states for the α-nitrogen crystal under the spin orbital coupling effect, and van der Waals interaction, and the evolution of the surface state for the two different crystal structures.
[50] H. Iwasawa, E. F. Schwier, M. Arita, A. Ino, H. Namatame, M. Taniguchi, Y. Aiura, and K. Shimada, Ultramicroscopy **182**, 85 (2017).
[51] A. A. Khajetoorians, D. Wegner, A. F. Otte, and I. Swart, Nat. Rev. Phys. **1**, 703 (2019).
[52] T. A. Cochran, I. Belopolski, K. Manna, M. Yahyavi, Y. Liu, D. S. Sanchez, Z.-J. Cheng, X. P. Yang, D. Multer, J.-X. Yin, H. Borrmann, A. Chikina, J. A. Krieger, J. Sánchez-Barriga, P. Le Fèvre, F. Bertran, V. N. Strocov, J. D. Denlinger, T.-R. Chang, S. Jia *et al.*, Phys. Rev. Lett. **130**, 066402 (2023).